Available online at www.sciencedirect.com
ScienceDirect
Journal of the European Ceramic Society 31 (2011) 3063–3071
www.elsevier.com/locate/jeurceramsoc

Investigation of nanodomain pattern and piezoelectric behavior of mixed phases in epitaxial $BiFeO_3$ films

H.Y. Kuo [a], Y.C. Shu [b,*], H.Z. Chen [b], C.J. Hsueh [b], C.H. Wang [c], Y.H. Chu [c]

[a] *Department of Civil Engineering, National Chiao Tung University, Hsinchu 300, Taiwan, ROC*
[b] *Institute of Applied Mechanics, National Taiwan University, Taipei 106, Taiwan, ROC*
[c] *Department of Materials Science and Engineering, National Chiao Tung University, Hsinchu 300, Taiwan, ROC*

Available online 14 May 2011

Abstract

Mixed phases of rhombohedral and tetragonal ferroelectric variants have been recently observed to coexist through epitaxial constraints in bismuth ferrite films. They form stripe-like domain patterns with orientations closely parallel to the substrate edges and exhibit unusually large piezoelectric response in the stripe areas. Here a model is developed for explaining the peculiar domain orientations as well as the enhancement of piezoelectricity in the mixed phase. The former is determined by the relative magnitudes of elastic and depolarization energy, whereas the latter is ascribed to the strain-driven softening in dielectric stiffness. The predictions show the similar trend as those observed in recent experiments.

Keywords: Bismuth ferrite; Domain pattern; Epitaxial film; Piezoelectricity

1. Introduction

Multiferroic materials, which show simultaneous two or more types of ferroelectric, magnetic or elastic orderings, have been the focus of research due to their varieties of microstructural phenomena and macroscopic properties. [1,2,3,4] These make multiferroics particularly appealing not only because they have the properties of all parent compounds, but also because interactions between different orderings lead to additional functionalities. [5,6,7] For example, certain multiferroic materials exhibit strong magnetoelectric effect which is an ability to manipulate the magnetic state through an electric field or vice versa.[8] This makes them promising for a wide range of applications, such as electrically controlled microwave phase shifters, broadband magnetic field sensors, and magnetoelectric memory cells.[9,10]

Among all multiferroic materials, bismuth ferrite ($BiFeO_3$, BFO) is the only known single phase material which possesses the coexistence of ferroelectric and antiferromagnetic orders at room temperature. They are characterized by the ferroelectric Curie temperature around 830 ° C and antiferromagnetic Néel temperature around 370 °C.[11,12,13,14] The bulk BFO single crystal has been shown to possess a rhombohedral pervoskite structure at room temperature, with the spontaneous polarization along one of the eight psuedo-cubic ⟨1 1 1⟩ axes, rendering it eight ferroelectric variants.[10,11] Besides, it possesses a G-type antiferromagnetic ordering so that magnetic spins stay on (1 1 1) planes. Within a (1 1 1) plane, magnetic spins are ferromagnetically coupled, whereas they are antiferromagnetically coupled between adjacent (1 1 1) planes.[10,12] As a result, by combining its magnetoelectric coupling with the exchange bias in ferromagnetic materials, electric control of ferromagnetic ordering has been recently demonstrated,[15] and thus opens door for practical applications of multiferroics in spintronics.

BFO has recently received renewed interest for its large room temperature spontaneous polarization and strong piezoelectric response in epitaxial thin films.[1,3,4,16,17,18] The abnormally large piezoelectricity is in sharp contrast to the weak coupling observed earlier in its bulk counterpart.[19] Different from conventional lead-based perovskites such as $PbZr_{1-x}Ti_xO_3$ (PZT) and relaxors $Pb(Mg_{1/3}Nb_{2/3})O_3$–$PbTiO_3$ (PMN-PT) and $Pb(Zn_{1/3}Nb_{2/3})O_3$–$PbTiO_3$ (PZN-PT), BFO is lead-free and therefore is an environmentally friendly piezoelectric material for device engineering. Besides, in contrast to forming morphotropic phase boundary (MPB) produced by selective compositional mixing for maximizing electrical responses,[20,21,22,23] the enhancement of piezoelectricity in BFO is attributed to the aggressive strategy of developing strain-driven MPB imposed by the substrate.[24,25,26,27] This method

* Corresponding author.
E-mail address: yichung@iam.ntu.edu.tw (Y.C. Shu).

0955-2219/$ – see front matter © 2011 Elsevier Ltd. All rights reserved.
doi:10.1016/j.jeurceramsoc.2011.04.010

takes advantage of the fact that domains in BFO can be changed through the control of epitaxial constraints, giving rise to the coexistence of two phases across MPB.

Specifically, the parent ground state of a stress-free BFO is of a rhombohedral crystalline structure. A stress-induced phase transition can be initiated by a sufficiently large compressive strain, as observed in epitaxial BFO films grown on $LaAlO_3$ substrates.[28,24] Indeed, a tetragonal-like phase is grown at an early stage of film deposition, and with increasing film thickness, the phase is gradually changed to completely rhombohedral due to the relaxation of misfit strain. At the intermediate stage of film growth, the rhombohedral phase emerges and coexists with the tetragonal phase, forming a stable strain-driven MPB. Stripe-like contrast images are observed and identified as lamellar patterns where the rhombohedral and tetragonal domains alternate in layers separated by parallel planes, as shown in Fig. 1.[24] Unlike the chemical composition driven MPB where phase-separating interfaces are typically mosaic and irregularly oriented,[29] it is found that the normals to the strips are oriented within 15 degrees from the [1 0 0] and [0 1 0] axes, as illustrated by arrows in Fig. 1. Besides, the piezoelectric responses in the stripe areas are larger than those measured in the single phase areas. [27] Several attempts based on the first-principles calculations,[28,30,31,32] Landau–Devonshire phenomenological theory,[33,34,35,36,37] modified Heisenberg and transverse Ising model [38] and phase-field simulations[39,40,41] have been carried out to investigate the effect of epitaxial strain on the structure and property of BFO. However, all of these theoretical developments are not able to explain the specific domain orientations and unusual piezoelectric behavior of the MPB, and neither can we draw directly from those proposed for the compositional tailored systems such as the PZT family and relaxaors. This article proposes a model based on the constrained theory of ferroelectrics [42,43,44] for investigating these two issues. Some of the preliminary results have been briefly reported in a short letter.[45] Here the framework is systematically introduced with the emphasis on the role of electromechanical compatibility on domain orientations. Besides, the explanations of the appearance of metastable tetragonal phase and the enhanced piezoelectric effect of the mixed phases are presented in detail.

The plan of this article is organized as follows. First the free energy of a ferroelectric crystal is introduced in Section 2.1. It is employed to explain the formation of tetragonal phase through epitaxial constraints in Section 2.2 and estimate the domain orientations of stripe-like patterns in Section 2.3. The piezoelectric responses of the pure and mixed phases are studied in Section 2.4. The results are provided and discussed in Section 3, and the conclusions are drawn in Section 4.

2. Framework and formulation

2.1. Free energy of a ferroelectric

Let us consider a ferroelectric described by two state variables: strain $\boldsymbol{\varepsilon}$ and polarization $\mathbf{p}$. When it is subjected to an applied electric field $\mathbf{E}^0$, the potential energy $\mathcal{I}$ of a ferroelectric in the linearized version of the framework proposed by Shu and Bhattacharya [46] is

$$\mathcal{I}(\mathbf{p}) = \int_\Omega \left\{ A|\nabla \mathbf{p}|^2 + W(\boldsymbol{\varepsilon}, \mathbf{p}) + W^{\mathrm{d}}(\mathbf{p}) - \mathbf{E}^0 \cdot \mathbf{p} \right\} d\mathbf{x}, \quad (1)$$

where

$$\begin{aligned} &W(\boldsymbol{\varepsilon}, \mathbf{p}) = W^{\mathrm{a}}(\mathbf{p}) + W^{\mathrm{elas}}(\boldsymbol{\varepsilon}, \mathbf{p}), \\ &W^{\mathrm{elas}}(\boldsymbol{\varepsilon}, \mathbf{p}) = \frac{1}{2}\left[\boldsymbol{\varepsilon} - \boldsymbol{\varepsilon}^*(\mathbf{p})\right] \cdot \mathbf{C}\left[\boldsymbol{\varepsilon} - \boldsymbol{\varepsilon}^*(\mathbf{p})\right], \\ &W^{\mathrm{d}}(\mathbf{p}) = -\frac{1}{2}\mathbf{p} \cdot \mathbf{E}^d. \end{aligned} \quad (2)$$

Above in Eq. (1), the first term with $A > 0$, called the interfacial energy density, penalizes the changes in the field variable $\mathbf{p}$, and thus, is interpreted as the energetic cost of forming domain walls separating different polarized states. The second term $W(\boldsymbol{\varepsilon}, \mathbf{p})$ is the total anisotropy energy density describing the energetic penalty that the crystal has to pay if the field variables deviate from the ground states of energy. Typically, $W(\boldsymbol{\varepsilon}, \mathbf{p})$ is decomposed as the sum of W^{a} and W^{elas} as in Eq. (2), [39,40,47] where W^{a} is the anisotropy energy density whose minimizers offer various polarized ground states, and W^{elas} is the elastic energy density with $\mathbf{C}$ as elastic moduli and $\boldsymbol{\varepsilon}^*(\mathbf{p})$ as the transformation strain. The dependence of $\boldsymbol{\varepsilon}^*(\mathbf{p})$ on $\mathbf{p}$ is

$$\begin{aligned} \varepsilon^*_{11} &= Q_{11}p_1^2 + Q_{12}p_2^2 + Q_{12}p_3^2, \\ \varepsilon^*_{22} &= Q_{12}p_1^2 + Q_{11}p_2^2 + Q_{12}p_3^2, \\ \varepsilon^*_{33} &= Q_{12}p_1^2 + Q_{12}p_2^2 + Q_{11}p_3^2, \\ \varepsilon^*_{23} &= Q_{44}p_2p_3, \\ \varepsilon^*_{31} &= Q_{44}p_3p_1, \\ \varepsilon^*_{12} &= Q_{44}p_1p_2, \end{aligned} \quad (3)$$

where $Q_{ij} = Q_{ji}$ are the electrostrictive coefficients.[41,48] The third term in Eq. (1) is the depolarization energy density in association with the electric field $\mathbf{E}^d$ generated by the polarization of the material itself. The final term is the potential energy density due to the external electric field $\mathbf{E}^0$.

The state variable $\mathbf{p}$ is then obtained by minimizing Eq. (1). To this end, the strain and depolarization fields have to be solved first. The strain $\boldsymbol{\varepsilon}$ is acquired by solving the mechanical equilibrium equation under appropriate boundary conditions

$$\nabla \cdot \boldsymbol{\sigma} = \mathbf{0}, \qquad \boldsymbol{\sigma} = \mathbf{C}\left[\boldsymbol{\varepsilon} - \boldsymbol{\varepsilon}^*(\mathbf{p})\right], \quad (4)$$

where $\boldsymbol{\sigma}$ is the symmetric elastic stress. In the present case where the ferroelectric film is deposited on a cubic substrate, an in-plane constraint is imposed on the film such that

$$\langle \varepsilon_{11} \rangle = \varepsilon^0_{11}, \qquad \langle \varepsilon_{22} \rangle = \varepsilon^0_{22}, \qquad \langle \varepsilon_{12} \rangle = \varepsilon^0_{12}, \quad (5)$$

where $\langle \cdots \rangle$ represents the volume average, and ε^0_{11}, ε^0_{22}, and ε^0_{12} are the misfit strains determined by the relative difference of lattice constants between the substrate and the film. Meanwhile, the surface of the film is assumed to be traction free, such that

$$\langle \sigma_{13} \rangle = 0, \qquad \langle \sigma_{23} \rangle = 0, \qquad \langle \sigma_{33} \rangle = 0. \quad (6)$$

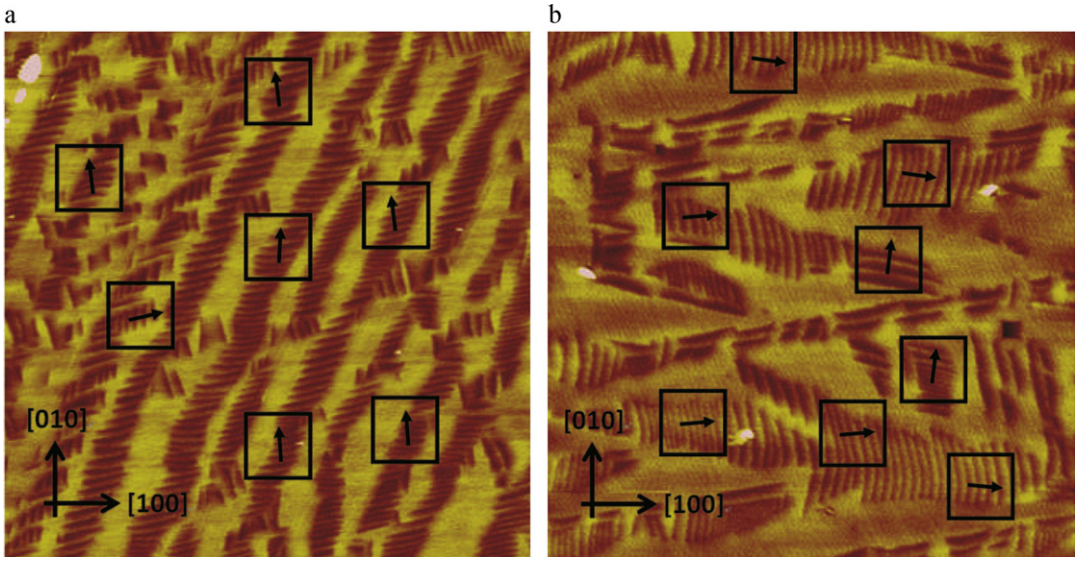

Fig. 1. Two AFM images showing a variety of lamellar patterns of the mixed rhombohedral (brown color) and tetragonal (yellow color) phases.[24] The arrows are marked to denote the in-plane directions of normals to the stripe-like domain patterns. They are oriented within around 15 degrees from the [1 0 0]/[0 1 0] axes. (For interpretation of the references to color in this figure legend, the reader is referred to the web version of the article.)

The depolarization field $\mathbf{E}^d$, on the other hand, can be decided by solving the Maxwell's equation

$$\nabla \cdot (-\epsilon_0 \nabla\phi + \mathbf{p}) = 0, \qquad \mathbf{E}^d = -\nabla\phi, \tag{7}$$

where ϵ_0 is the permittivity of free space.

For BFO at around room temperature, it has a stable rhombohedral phase with ⟨1 1 1⟩ eight polarized states, and a metastable tetragonal phase with ⟨0 0 1⟩ six polarized states. Its well structure of energy is schematically illustrated in Fig. 2. The well points of energy correspond to the ground states of ferroelectric variants expressed as $(\boldsymbol{\varepsilon}^*(\mathbf{p}_s), \mathbf{p}_s)$. Let the superscripts T and R represent the tetragonal and rhombohedral phases, respectively. The transformation strain and polarization of rhombohedral variants from Eq. (3) are given by

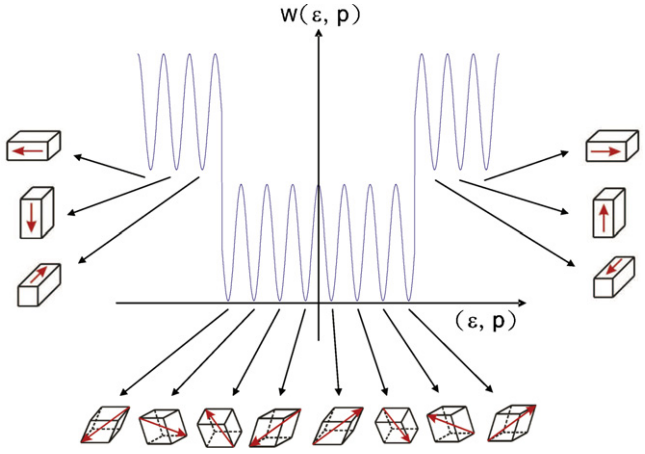

Fig. 2. A schematic representation of the multi-well structure of total anisotropy energy density $W(\boldsymbol{\varepsilon}, \mathbf{p})$ in the strain-polarization space.

$$\boldsymbol{\varepsilon}^*\left(\mathbf{p}_s^R\right) = \begin{pmatrix} Q_{11}+2Q_{12} & Q_{44} & Q_{44} \\ Q_{44} & Q_{11}+2Q_{12} & Q_{44} \\ Q_{44} & Q_{44} & Q_{11}+2Q_{12} \end{pmatrix} \left(P_s^R\right)^2,$$

$$\mathbf{p}_s^R = \frac{P_s^R}{\sqrt{3}} \begin{pmatrix} 1 \\ 1 \\ 1 \end{pmatrix}, \tag{8}$$

and permutations for other variants. The tetragonal variants are given by

$$\boldsymbol{\varepsilon}^*\left(\mathbf{p}_s^T\right) = \begin{pmatrix} Q_{12} & 0 & 0 \\ 0 & Q_{12} & 0 \\ 0 & 0 & Q_{11} \end{pmatrix} \left(P_s^T\right)^2, \qquad \mathbf{p}_s^T = P_s^T \begin{pmatrix} 0 \\ 0 \\ 1 \end{pmatrix}, \tag{9}$$

and permutations for other variants. Here P_s^R and P_s^T are the magnitudes of the ground states of polarization for rhombohedral and tetragonal phases, respectively.

2.2. Tetragonal phase

The tetragonal phase, in fact, does not appear naturally in a reference crystal. However, it has been observed to emerge through epitaxial constraints in BFO films. Indeed, it can be explained by comparing the magnitudes of energy for two different polarized ground states $\mathbf{p}_s^R$ and $\mathbf{p}_s^T$ subject to compressive constraint. From Eq. (1) under $\mathbf{E}^0 = \mathbf{0}$, the tetragonal phase might appear if

$$W^{\mathrm{a}}(\mathbf{p}_s^T) + W^{\mathrm{elas}}\left(\boldsymbol{\varepsilon}^0, \mathbf{p}_s^T\right) < W^{\mathrm{a}}(\mathbf{p}_s^R) + W^{\mathrm{elas}}\left(\boldsymbol{\varepsilon}^0, \mathbf{p}_s^R\right), \tag{10}$$

where $\boldsymbol{\varepsilon}^0$ is the overall misfit strain such that its in-plane components are equal to those in Eq. (5) and out-of-plane components are those satisfying the plane-stress condition in Eq. (6). From

Eq. $(2)_2$, the elastic energy density can be decomposed into three terms:

$$\frac{1}{2}\mathbf{C}\boldsymbol{\varepsilon}^0\cdot\boldsymbol{\varepsilon}^0,\ \frac{1}{2}\mathbf{C}\boldsymbol{\varepsilon}^*(\mathbf{p})\cdot\boldsymbol{\varepsilon}^*(\mathbf{p}),\ -\mathbf{C}\boldsymbol{\varepsilon}^0\cdot\boldsymbol{\varepsilon}^*(\mathbf{p}).$$

The first term is the same for both phases and therefore, is irrelevant. As the polarization is restricted to the well points of energy, the difference of the second term for different phases $((1/2)\mathbf{C}\boldsymbol{\varepsilon}^*(\mathbf{p}_s^R)\cdot\boldsymbol{\varepsilon}^*(\mathbf{p}_s^R)-(1/2)\,\mathbf{C}\boldsymbol{\varepsilon}^*(\mathbf{p}_s^T)\cdot\boldsymbol{\varepsilon}^*(\mathbf{p}_s^T))$ is fixed and independent of misfit strain. Finally, let $\boldsymbol{\sigma}^0=\mathbf{C}\boldsymbol{\varepsilon}^0$ denote the misfit stress. Thus, the third term can be written as $(-\boldsymbol{\sigma}^0\cdot\boldsymbol{\varepsilon}^*(\mathbf{p}))$, representing the equivalent mechanical potential energy density. For BFO films grown on $LaAlO_3$ substrates, the misfit strains $\varepsilon_{11}^0=\varepsilon_{22}^0<0$ and $\varepsilon_{12}^0=0$. This provides $\sigma_{11}^0=\sigma_{22}^0<0$ and $\sigma_{12}^0=0$. Further, for BFO crystals, $Q_{11}=-2Q_{12}$ and $Q_{12}<0$.[41] Thus, from Eq. (8), $\boldsymbol{\varepsilon}^*(\mathbf{p}_s^R)$ is completely pure shear, giving rise to $\boldsymbol{\sigma}^0\cdot\boldsymbol{\varepsilon}^*(\mathbf{p}_s^R)=0$. On the other hand, for the tetragonal variants as in Eq. (9) and its permutations,

$$-\boldsymbol{\sigma}^0\cdot\boldsymbol{\varepsilon}^*(\mathbf{p}_s^T)=\begin{cases}-2\sigma_{11}^0Q_{12}<0 & \text{if } \mathbf{p}_s^T \text{ is parallel to[0 0 1]},\\ \sigma_{11}^0Q_{12}>0 & \text{if } \mathbf{p}_s^T \text{ is parallel to[1 0 0]},\\ \sigma_{11}^0Q_{12}>0 & \text{if } \mathbf{p}_s^T \text{ is parallel to[0 1 0]}.\end{cases}\tag{11}$$

Therefore, from Eqs. (10) and (11), the energy barrier $(W^{\mathrm{a}}(\mathbf{p}_s^T)-W^{\mathrm{a}}(\mathbf{p}_s^R))$ can be overcome by $(W^{\mathrm{elas}}(\boldsymbol{\varepsilon}^0,\mathbf{p}_s^R)-W^{\mathrm{elas}}(\boldsymbol{\varepsilon}^0,\mathbf{p}_s^T))$ if the tetragonal variant is chosen to be polarized normal to the film under a sufficiently large compressive misfit stress. This gives tetragonal phase oriented normal to the film as a low energy minimizer, as observed by the experiment.[24]

2.3. Mixtures of the rhombohedral and tetragonal phases

As the BFO film grows, the strain relaxation of misfit furnishes an opportunity for the emergence of the rhombohedral phase. The stripe-like domains shown in Fig. 1 motivate us to postulate the lamellar patterns for the mixed phase. It consists of alternating tetragonal and rhombohedral ferroelectric variants separated by interfaces with unit normal $\mathbf{n}$, as illustrated in Fig. 3 where f is the volume fraction of the rhombohedral phase.

In most ferroelectrics, the induced magnitude of polarization is much smaller than that of spontaneous one, and therefore, the constrained theory of ferroelectrics is adopted assuming that the energy-well structure is steep away from the ground states.[42,43,44,49] As such, the polarization $\mathbf{p}$ is restricted to one of the well points of energy; i.e., $\mathbf{p}=\mathbf{p}_s^T(\mathbf{p}_s^R)$ in the region occupied by the tetragonal (rhombohedral) phase. As a result, the energy barrier $(W^{\mathrm{a}}(\mathbf{p}_s^T)-W^{\mathrm{a}}(\mathbf{p}_s^R))$ from the anisotropy energy density is independent of the laminate orientation $\mathbf{n}$. In addition, the consideration of equilibrium domain configurations rather than domain evolution suggests the neglect of interfacial energy. Under these two assumptions and from Eq. (1) at the absence of an external electric field, the orientation $\mathbf{n}$ depends only on W^{elas} and W^{d} whose calculations are described next.

Consider the elastic energy first which can be achieved once the strain fields in the laminate are determined. Let $\boldsymbol{\varepsilon}^*(\mathbf{p}_s^R)$ and $\boldsymbol{\varepsilon}^*(\mathbf{p}_s^T)$ be the transformation strains and $\boldsymbol{\varepsilon}^R$ and $\boldsymbol{\varepsilon}^T$ be the strains in the laminate regions occupied by the rhombohedral and tetragonal phases, respectively. As the displacement is continuous across the phase-separating interface, strain compatibility requires

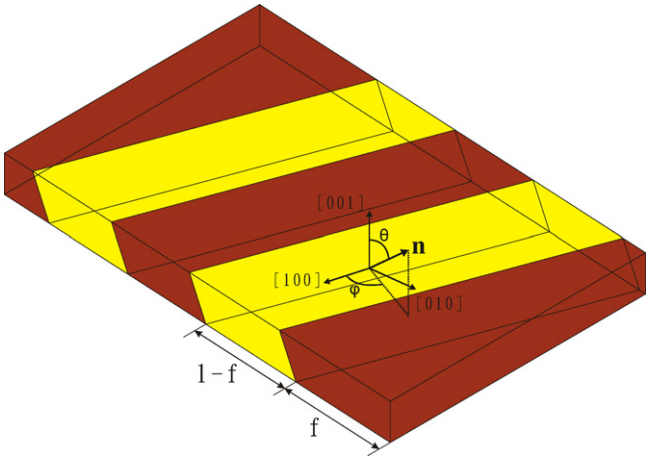

Fig. 3. A schematic representation of the lamellar pattern consisting of alternating tetragonal (yellow color) and rhombohedral (brown color) phases. The interfacial normal $\mathbf{n}$ is presented by angles θ and φ, as in Eq. (18). (For interpretation of the references to color in this figure legend, the reader is referred to the web version of the article.)

$$\boldsymbol{\varepsilon}^R-\boldsymbol{\varepsilon}^T=\mathbf{a}\otimes\mathbf{n}+\mathbf{n}\otimes\mathbf{a},\tag{12}$$

for some vector $\mathbf{a}$.[46] Here $(\mathbf{a}\otimes\mathbf{n})_{ij}=a_in_j$. Further, the absence of surface forces gives the continuity of the normal stress across the interface. This delivers

$$[[\boldsymbol{\sigma}]]\cdot\mathbf{n}=(\boldsymbol{\sigma}^R-\boldsymbol{\sigma}^T)\cdot\mathbf{n}=\mathbf{0},\tag{13}$$

where the notation $[[\cdots]]$ denotes the jump across the interface $\mathbf{n}$. Assume both phases own the identical elastic modulus $\mathbf{C}$ with isotropy property. The strain fields $\boldsymbol{\varepsilon}^R$ and $\boldsymbol{\varepsilon}^T$ therefore are obtained through the strain compatibility in Eq. (12), stress interface condition in Eq. (13), and boundary conditions in both Eqs. (5) and (6). These give

$$\begin{aligned}\boldsymbol{\varepsilon}^R&=\langle\boldsymbol{\varepsilon}\rangle+(1-f)(\mathbf{a}\otimes\mathbf{n}+\mathbf{n}\otimes\mathbf{a}),\\ \boldsymbol{\varepsilon}^T&=\langle\boldsymbol{\varepsilon}\rangle-f(\mathbf{a}\otimes\mathbf{n}+\mathbf{n}\otimes\mathbf{a}),\\ \mathbf{a}&=\left(\mathbf{I}-\frac{C_{12}+C_{44}}{C_{12}+2C_{44}}\mathbf{n}\otimes\mathbf{n}\right)\left[\boldsymbol{\varepsilon}^*(\mathbf{p}_s^R)-\boldsymbol{\varepsilon}^*(\mathbf{p}_s^T)\right]\mathbf{n},\end{aligned}\tag{14}$$

where $\langle\boldsymbol{\varepsilon}\rangle=f\boldsymbol{\varepsilon}^R+(1-f)\boldsymbol{\varepsilon}^T$, $\mathbf{I}$ is the identity tensor, C_{ij} are the components of isotropic elastic tensor in terms of Voigt notation. The derivation of Eq. (14) is provided in Appendix.

Next, the depolarization fields $\mathbf{E}^{d,R}$ and $\mathbf{E}^{d,T}$ of rhombohedral and tetragonal phases in the laminate are determined as follows. Note that the ground states of polarization are previously assumed in deriving the strain fields. To account for the induced polarization, the constrained model is modified by including the dielectric effect. Indeed, electric displacement $\mathbf{D}$ is rewritten as $\mathbf{D}=\epsilon\mathbf{E}^d+\mathbf{p}_s$ where ϵ is the permittivity of material.[50] The normal components of electric displacement has to be continuous across the interface due to the absence of free charges. Therefore,

we have

$$[[\epsilon \mathbf{E}^d + \mathbf{p}_s]] \cdot \mathbf{n} = \left\{ \left(\epsilon^R \mathbf{E}^{d,R} + \mathbf{p}_s^R \right) - \left(\epsilon^T \mathbf{E}^{d,R} + \mathbf{p}_s^T \right) \right\} \cdot \mathbf{n} = 0, \tag{15}$$

where ϵ^R and ϵ^T are permittivity coefficients of rhombohedral and tetragonal phases. In addition, the continuity of electric potential across the interface $\mathbf{n}$ requires

$$[[\mathbf{E}^d]] = \mathbf{E}^{d,R} - \mathbf{E}^{d,T} = k\mathbf{n}, \tag{16}$$

where k is an unknown constant needed to be decided. Finally, note that the depolarization field from the contribution of average of polarization is irrelevant. This gives $\langle \mathbf{E}^d \rangle = \langle -\nabla\phi \rangle = \mathbf{0}$ due to the periodicity of laminate. Combining this fact with Eqs. (15) and (16) provides

$$\begin{aligned} \mathbf{E}^{d,R} &= \frac{f-1}{\bar{\epsilon}} \left[\mathbf{n} \cdot \left(\mathbf{p}_s^R - \mathbf{p}_s^T \right) \right] \mathbf{n}, \\ \mathbf{E}^{d,T} &= \frac{f}{\bar{\epsilon}} \left[\mathbf{n} \cdot \left(\mathbf{p}_s^R - \mathbf{p}_s^T \right) \right] \mathbf{n}, \end{aligned} \tag{17}$$

where $\bar{\epsilon} = (1-f)\epsilon^R + f\epsilon^T$.

From Eqs. (14) and (17), it is clear that the magnitudes of elastic and polarization energy depend only on the phase differences of state variables $(\boldsymbol{\varepsilon}^*(\mathbf{p}_s^R) - \boldsymbol{\varepsilon}^*(\mathbf{p}_s^T))$ and $(\mathbf{p}_s^R - \mathbf{p}_s^T)$. The former is related to strain compatibility for reducing intrinsic stress across certain interface with normal $\mathbf{n}'$, while the latter is related to electric compatibility for avoiding charge accumulation on the phase boundary with normal $\mathbf{n}''$. In general, $\mathbf{n}'$ and $\mathbf{n}''$ are distinct unless certain conditions are imposed. According to Shu and Bhattacharya's ferroelectric theory,[46] $\mathbf{n}'$ and $\mathbf{n}''$ coincide if the ferroelectric state variables are symmetry related variants. Unfortunately, the ground states of rhombohedral $(\boldsymbol{\varepsilon}^*(\mathbf{p}_s^R), \mathbf{p}_s^R)$ and tetragonal $(\boldsymbol{\varepsilon}^*(\mathbf{p}_s^T), \mathbf{p}_s^T)$ phases are not symmetry related, giving rise to no correlation between elastic and depolarization energy.

The optimal orientation $\mathbf{n}$ is then readily determined by energy minimization. Specifically, we seek to find the interface normal

$$\mathbf{n} = (\sin\theta\,\cos\varphi,\ \sin\theta\,\sin\varphi,\ \cos\theta) \tag{18}$$

that minimizes $(W^{\text{elas}} + W^{\text{d}})$. Here θ is measured from the normal to the film, and the in-plane angle φ is measured from the [1 0 0] axis, as illustrated in Fig. 3. Although there are a variety of methods for solving this highly nonlinear problem numerically,[51] all of these approaches find the local optimum rather than the global minimum that we seek. Therefore we resort to the brute-force optimization by creating fine grids of Euler angles (θ, φ), and examine the values of energy on these grids for searching minimum energy.

2.4. Piezoelectricity

We now turn to the piezoelectric responses of the pure and mixed phases of strained BFO thin films. The out-of-plane displacement is measured under the electric field normal to the film. Thus, the piezoelectric coupling coefficient is defined as

$$d_{33} = \frac{d\langle \varepsilon_{33} \rangle}{dE_3^0} = \sum_{i=1}^{3} \frac{\partial \langle \varepsilon_{33} \rangle}{\partial p_i} \frac{\partial p_i}{\partial E_3^0}, \tag{19}$$

where $\langle \varepsilon_{33} \rangle$ is the average strain normal to the film and is given by Eq. (A.1). The piezoelectric coefficient d_{33} can be achieved once the polarization induced by an electric field is determined; i.e., $(\partial p_i / \partial E_3^0)$ has to be provided first. Indeed, consider the thermodynamic driving force derived from the total free energy $\mathcal{I}(\mathbf{p})$ in Eq. (1). Minimizing $\mathcal{I}(\mathbf{p})$ under the application of an electric field gives [44,52]

$$\frac{\partial W^{\text{a}}(\mathbf{p})}{\partial \mathbf{p}} - \boldsymbol{\sigma} \cdot \frac{\partial \boldsymbol{\varepsilon}^*(\mathbf{p})}{\partial \mathbf{p}} - \mathbf{E}^0 - \mathbf{E}^{\text{d}} = 0. \tag{20}$$

Above the first term is interpreted as the electric field induced by the change of polarization deviating from the polarized ground state. The second term is the effective electric field induced by the stress which originates from the external constraint due to the misfit strain and the internal constraint due to the incompatibility in transformation strains across the interface. As revealed by experiments, the polarization in the two-phase region deviates little from its polarized ground state. Thus, the anisotropy energy density is approximated to be

$$W^{\text{a}}(\mathbf{p}) = \frac{1}{2} \left(\mathbf{p} - \mathbf{p}_s^R \right) \cdot \left(\epsilon^R \mathbf{I} - \epsilon_0 \mathbf{I} \right)^{-1} \left(\mathbf{p} - \mathbf{p}_s^R \right) \tag{21}$$

for $\mathbf{p}$ near the rhombohedral phase and

$$W^{\text{a}}(\mathbf{p}) = \frac{1}{2} \left(\mathbf{p} - \mathbf{p}_s^T \right) \cdot \left(\epsilon^T \mathbf{I} - \epsilon_0 \mathbf{I} \right)^{-1} \left(\mathbf{p} - \mathbf{p}_s^T \right) \tag{22}$$

for $\mathbf{p}$ close to the tetragonal phase.

3. Results and discussion

The framework developed in the previous section is now applied to investigate the orientations of stripe-like domain patterns and the piezoelectric response of the mixed phase in a strained BFO film. The relevant material properties of bismuth ferrite are listed below: $P_s^R = 0.09\,\text{C m}^{-2}$, $P_s^T = 0.55\,\text{C m}^{-2}$, electrostrictive coefficients $Q_{11} = 0.032\,\text{m}^4\,\text{C}^{-2}$, $Q_{12} = -0.016\,\text{m}^4\,\text{C}^{-2}$, $Q_{44} = 0.01\,\text{m}^4\,\text{C}^{-2}$, isotropic elastic moduli $C_{12} = 162\,\text{GPa}$, $C_{44} = 143\,\text{GPa}$, and permittivity constants $\epsilon^R = 120\epsilon_0$, $\epsilon^T = 70\epsilon_0$.[34] The volume fraction of the rhombohedral phase is observed to be $f = 0.4$.[24]

As explained in Section 2.2, the tetragonal variant polarized normal to the film is an energy minimizer under compressive misfit stress. Thus, $\mathbf{p}_s^T = P_s^T[0\,0\,1]$ is chosen to represent the polarized variant in the tetragonal phase. However, there are four possible polarized states for rhombohedral variants due to symmetry. Suppose they are taken as $\mathbf{p}_s^R = P_s^R[1\,1\,1]$ or $\mathbf{p}_s^R = P_s^R[\bar{1}\,\bar{1}\,1]$. The magnitudes of elastic and depolarization energy are obtained by substituting Eqs. (14) and (17) into Eq. (2). The minimization of the sum of these two over all possible $\mathbf{n}$, as presented by θ and φ in Eq. (18), determines the optimal

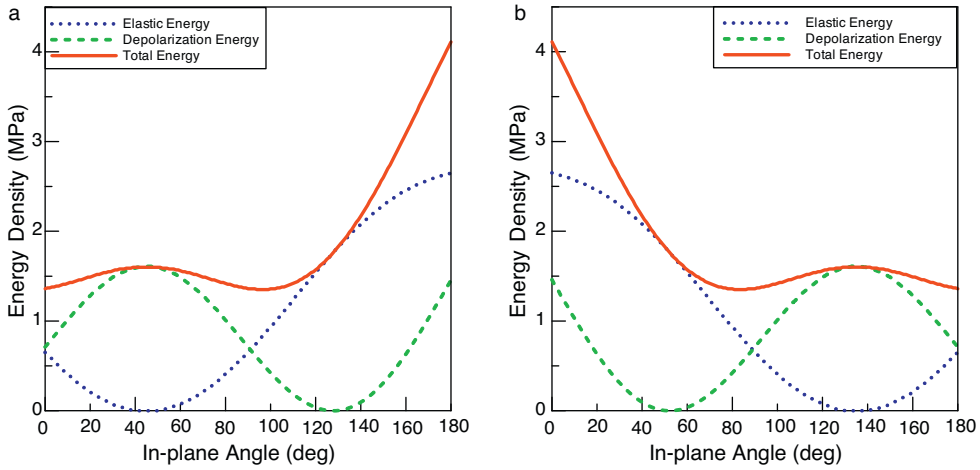

Fig. 4. Elastic, depolarization and total energy of the mixed phase for various orientations of the laminate. Note that a fixed reference value of energy is taken and removed from the elastic and total energy densities for clearness. (a) R-phase is chosen along the polarized direction [111] or [$\bar{1}\bar{1}$1]. (b) R-phase is chosen along the polarized direction [$\bar{1}$11] or [1$\bar{1}$1].

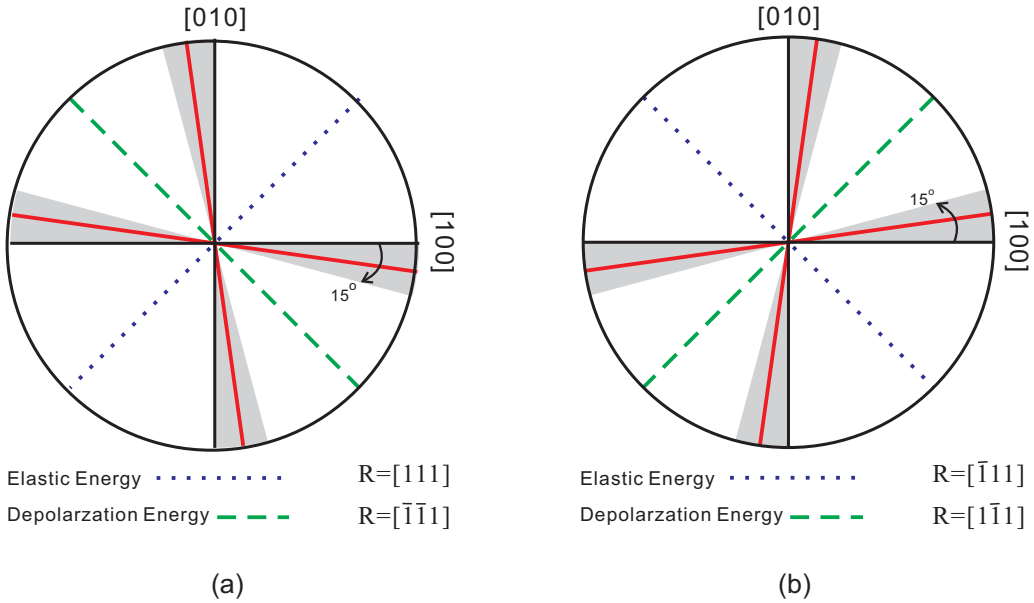

Fig. 5. The top view of optimal orientations of lamellar pattern of the mixed phase for the consideration of elastic (blue lines), depolarization (green lines) and total energy (red lines). The shadow regions represent the spread of observed orientations of stripe-like pattern. (a) R-phase is chosen along the polarized direction [1 1 1] or [$\bar{1}$ $\bar{1}$ 1]. (b) R-phase is chosen along the polarized direction [$\bar{1}$ 1 1] or [1 $\bar{1}$ 1]. (For interpretation of the references to color in this figure legend, the reader is referred to the web version of the article.)

orientations of laminates. The result shows that the minimum of $(W^{\text{elas}} + W^{\text{d}})$ occurs at $(\theta, \varphi) = (18°, 96°)$, $(18°, 354°)$ for P_s^R[1 1 1] and $(18°, 174°)$, $(18°, 276°)$ for P_s^R[$\bar{1}$ $\bar{1}$ 1], as listed in Table 1. The dependence of the total, elastic, and depolarization energy densities of the mixed phases at $\theta = 18°$ on the in-plane angle φ is shown in Fig. 4(a). It shows that the elastic energy due to incompatible strains of mixed phases is minimized at the in-plane angle of 45° (see the blue line in Fig. 4(a) and Fig. 5(a)), while the depolarization energy is minimized at around 135° (see the green line in Fig. 4(a) and Fig. 5(a)). Note that these two angles are nearly orthogonal to each other and are not sensitive to the material properties including elastic, electrostrictive and permittivity constants. However, the optimal laminate orientations depend on the relative magnitudes of elastic and depolarization energy. Thus, it is expected to fall between these two in-plane angles. Indeed, the calculation shows that the minimum energy occurs at an in-plane angle near the [1 0 0] and [0 1 0] axes, as demonstrated by the red lines in Fig. 4(a) and Fig. 5(a), where the in-plane angles are 6 degrees deviating from [1 0 0] and [0 1 0]. Similarly, consider another choice of

Table 1
The optimal orientations of the laminate for different choices of rhombohedral variants at $\theta = 18°$.

$\mathbf{p}_s^R$	[1 1 1]	[$\bar{1}$ 1 1]	[1 $\bar{1}$ 1]	[$\bar{1}$ $\bar{1}$ 1]
φ	96°	84°	6°	174°
	354°	186°	264°	276°

Table 2
Piezoelectric coupling coefficients d_{33} for pure and mixed phases obtained from the experiment and the model.

d_{33} (pm/V)	T	R	Mixed T/R
Experiment	28	61	96
Model	45	63	116

the polarized states for the rhombohedral ferroelectric variants. They are taken as $P_s^R[\bar{1}\,1\,1]$ or $P_s^R[1\,\bar{1}\,1]$. In this case, the in-plane angle minimizing the elastic energy is 135° from [1 0 0] axis (see the blue line in Fig. 4(b) and Fig. 5(b)), whereas it is around 45° from [1 0 0] axis for minimizing the depolarization energy (see the green line in Fig. 4(b) and Fig. 5(b)). The optimal orientations are provided in Table 1. As expected, they are very close to [1 0 0] or [0 1 0] axes from the top view, as shown by the red lines in Fig. 5(b). The prediction is in good agreement with that observed in recent experiment, as demonstrated by the marked arrows in Fig. 1. These arrows represent the in-plane normals of stripe-like domain patterns. They are regularly oriented within 15 degrees around [1 0 0]/[0 1 0] axes, as in the shadow regions illustrated in Fig. 5.

Next let us investigate the piezoelectric responses of the pure and mixed phases. Table 2 lists the measured data of d_{33} from experiments for pure tetragonal, pure rhombohedral and mixture of these two phases in an epitaxial constrained BFO thin film.[27] The piezoelectric coupling coefficients d_{33} are around 30, 60 and 100 pm/V, respectively. The magnitude of d_{33} in the mixed phase is larger than that in the pure tetragonal phase since the rhombohedral phase has a higher permittivity coefficient than that of the tetragonal phase ($\epsilon^R > \epsilon^T$). Surprisingly it is also higher than that in the pure rhombohedral phase, violating the fact that the effective constant of mixed phase is bounded by those of the pure phases.

To explain it, consider the second term of Eq. (20) representing the stress-induced electric field. The stress can be decomposed into two terms

$$\boldsymbol{\sigma} = \boldsymbol{\sigma}^0 + \boldsymbol{\sigma}', \tag{23}$$

where $\boldsymbol{\sigma}^0$ is the constant stress resulting from the misfit strain $\boldsymbol{\varepsilon}^0$ as in Eq. (5), and $\boldsymbol{\sigma}'$ is the inhomogeneous stress resulting from the incompatible transformation strain $\boldsymbol{\varepsilon}^*$ as in Eq. (3) of the mixed phase. Note that $\boldsymbol{\sigma}'$ satisfies $\langle\varepsilon_{11}\rangle = \langle\varepsilon_{22}\rangle = \langle\varepsilon_{12}\rangle = 0$ due to superposition. As a result, $\boldsymbol{\sigma}^0$ is one order of magnitude larger than that of $\boldsymbol{\sigma}'$ since the measured misfit strains are around the order of 10^{-2} whereas the transformation strains are order of 10^{-3}. Therefore, the leading coefficient in Eq. (20) for the component p_3 is approximated to be

$$\left(-\sigma_{11}^0 \frac{\partial \varepsilon_{11}^*(\mathbf{p})}{\partial p_3} - \sigma_{22}^0 \frac{\partial \varepsilon_{22}^*(\mathbf{p})}{\partial p_3} - 2\sigma_{12}^0 \frac{\partial \varepsilon_{12}^*(\mathbf{p})}{\partial p_3}\right) / p_3 = -4\sigma_{11}^0 Q_{12}. \tag{24}$$

This term is negative since $\sigma_{11}^0 < 0$ and $Q_{12} < 0$, giving rise to the softening in relative permittivity stiffness (ϵ^{-1}). It in turn increases the effective dielectric constant, causing the enhancement of d_{33} as can be seen from Eq. (19). However, such a softening effect depends on the magnitude of misfit stress which is continuously relaxed as the film grows. For instance, the appearance of pure rhombohedral, mixed and tetragonal phases takes place at compressive strains lower than 3%, between 3 and 4% and larger than 4%.[24] Hence, the softening in permittivity stiffness is much more pronounced in the mixed phase than that of the pure rhombohedral phase. Indeed, with parameters listed above, the piezoelectric coefficients d_{33} obtained from Eq. (19) are 45, 63 and 116 pm/V for the tetragonal, rhombohedral and mixed phases. With comparison to Table 2, these predicted results show the similar trend as those observed in experiments, confirming the enhancement of piezoelectric response is mainly attributed to the softening of the dielectric stiffness. This softening arises from the stress-induced electric field from the change of out-of-plane polarization, as can be seen from Eq. (24).

4. Conclusions

A framework based on the constrained model of ferroelectrics is systematically developed for predicting the domain orientations and explaining the piezoelectric response of the mixed phase in an epitaxial strained bismuth ferrite film. First it is shown that the tetragonal variant polarized normal to the film is a low energy state under a sufficiently large compressive misfit stress. Next, the rhombohedral phase emerges and coexists with the tetragonal phase due to the relaxation of misfit strain. Both phases alternate in layers forming stripe-like patterns with orientations nearly parallel to the edges of the substrate. It is shown that these peculiar orientations are the consequence of competition between elastic and depolarization energy. Finally, the effective piezoelectric coefficients of the pure and mixed phases are estimated. It is shown that the abnormally strong piezoelectric response of the mixed phase is ascribed to the strain-driven softening of dielectric stiffness. This softening arises from the effective electric field induced by in-plane stress from the change of out-of-plane polarization. The results are compared to recent experiments and show reasonable agreement.

Acknowledgements

The supports from the National Science Council (NSC-97-2221-E-002-125-MY3, NSC 98-2211-E009-095 and NSC-99-2811-M-009-003) are gratefully acknowledged.

Appendix A. Derivation of $\boldsymbol{\varepsilon}^R$ and $\boldsymbol{\varepsilon}^T$ in Eq. (14)

From the kinematic compatibility condition as in Eq. (12) and the definition of average strain $\langle\boldsymbol{\varepsilon}\rangle = f\boldsymbol{\varepsilon}^R + (1-f)\boldsymbol{\varepsilon}^T$, the strains $\boldsymbol{\varepsilon}^T$ and $\boldsymbol{\varepsilon}^R$ can be expressed as in Eq. (14) with two unknowns $\langle\boldsymbol{\varepsilon}\rangle$ and $\mathbf{a}$. The in-plane components of $\langle\boldsymbol{\varepsilon}\rangle$ are given by Eq. (5), while its out-of-plane components are obtained from the plane-stress condition as in Eq. (6) and the isotropy of elastic modulus $\mathbf{C}$. These give

$$\begin{aligned} &\langle\varepsilon_{32}\rangle = \langle\varepsilon_{32}^*\rangle, \qquad \langle\varepsilon_{31}\rangle = \langle\varepsilon_{31}^*\rangle, \\ &\langle\varepsilon_{33}\rangle = \langle\varepsilon_{33}^*\rangle - \frac{C_{12}}{C_{12}+2C_{44}}\left[\varepsilon_{11}^0 + \varepsilon_{22}^0 - \langle\varepsilon_{11}^*\rangle - \langle\varepsilon_{22}^*\rangle\right], \end{aligned} \tag{A.1}$$

where $\langle \boldsymbol{\varepsilon}^* \rangle = f\boldsymbol{\varepsilon}^*(\mathbf{p}_s^R) + (1-f)\boldsymbol{\varepsilon}^*(\mathbf{p}_s^T)$. Another unknown vector $\mathbf{a}$ is determined as follows.

Substituting Eqs. (4) and (12) into Eq. (13) provides

$$\left\{\mathbf{C}\left[(\mathbf{a}\otimes\mathbf{n}+\mathbf{n}\otimes\mathbf{a}) - \left(\boldsymbol{\varepsilon}^*\left(\mathbf{p}_s^R\right) - \boldsymbol{\varepsilon}^*\left(\mathbf{p}_s^T\right)\right)\right]\right\}\mathbf{n} = 0. \quad \text{(A.2)}$$

Above can be simplified using the isotropy of $\mathbf{C}$. This gives

$$\begin{aligned}&[(C_{12}+C_{44})\,\mathbf{n}\otimes\mathbf{n} + C_{44}\mathbf{I}]\,\mathbf{a}\\ &= \frac{C_{12}}{2} Tr\left[\boldsymbol{\varepsilon}^*\left(\mathbf{p}_s^R\right) - \boldsymbol{\varepsilon}^*\left(\mathbf{p}_s^T\right)\right]\mathbf{n}\\ &\quad + C_{44}\left[\boldsymbol{\varepsilon}^*\left(\mathbf{p}_s^R\right) - \boldsymbol{\varepsilon}^*\left(\mathbf{p}_s^T\right)\right]\mathbf{n}, \end{aligned} \quad \text{(A.3)}$$

where $Tr[A_{ij}] = \sum_{i=1}^{3} A_{ii}$. Note that from Eq. (3)

$$Tr\left[\boldsymbol{\varepsilon}^*(\mathbf{p})\right] = 0$$

since $Q_{11} = -2Q_{12}$. Thus, Eq. (A.3) becomes

$$\mathbf{a} = C_{44}[(C_{12}+C_{44})\,\mathbf{n}\otimes\mathbf{n} + C_{44}\mathbf{I}]^{-1}\left[\boldsymbol{\varepsilon}^*\left(\mathbf{p}_s^R\right) - \boldsymbol{\varepsilon}^*\left(\mathbf{p}_s^T\right)\right]\mathbf{n}.$$

This completes deriving Eq. (14) since

$$C_{44}[(C_{12}+C_{44})\,\mathbf{n}\otimes\mathbf{n} + C_{44}\mathbf{I}]^{-1} = \mathbf{I} - \frac{C_{12}+C_{44}}{C_{12}+2C_{44}}\mathbf{n}\otimes\mathbf{n}.$$

References

1. Wang J, Neaton JB, Zheng H, Nagarajan V, Ogale SB, Liu B, et al. Epitaxial $BiFeO_3$ multiferroic thin film heterostructures. *Science* 2003;**299**:1719–22.
2. Lottermoser T, Lonkai T, Amann U, Hohlwein D, Ihringer J, Fiebig M. Magnetic phase control by an electric field. *Nature* 2004;**430**:541–4.
3. Ramesh R, Spaldin NA. Multiferroics: progress and prospects in thin films. *Nature Materials* 2007;**6**:21–9.
4. Catalan G, Scott JF. Physics and applications of bismuth ferrite. *Advanced Materials* 2009;**21**:2463–85.
5. Fiebig M. Revival of the magnetoelectric effect. *Journal of Physics D: Applied Physics* 2005;**38**:R123–52.
6. Spaldin NA, Fiebig M. The renaissance of magnetoelectric multiferroics. *Science* 2005;**309**:391–2.
7. Eerenstein W, Mathur ND, Scott JF. Multiferroic and magnetoelectric materials. *Nature* 2006;**442**:759–65.
8. Fiebig M, Lottermoser T, Frohlich D, Golstev AV, Pisarev RV. Observation of coupled magnetic and electric domains. *Nature* 2002;**419**:818–20.
9. Hur N, Park S, Sharma PA, Ahn JS, Guha S, Cheong SW. Electric polarization reversal and memory in a multiferroic material induced by magnetic fields. *Nature* 2004;**429**:392–5.
10. Zhao T, Scholl A, Zavaliche F, Lee K, Barry M, Doran A, et al. Electrical control of antiferromagnetic domains in multiferroic $BiFeO_3$ films at room temperature. *Nature Materials* 2006;**5**:823–9.
11. Michel C, Moreau JM, Achenbach GD, Gerson R, James WJ. The atomic structure of $BiFeO_3$. *Solid State Communications* 1969;**7**:701–4.
12. Fischer P, Polomska M, Sosnowska I, Szymanski M. Temperature dependence of the crystal and magnetic structure of $BiFeO_3$. *Journal of Physics C: Solid State Physics* 1980;**13**:1931–40.
13. Murashav VA, Rakov DN, Ionov VM, Dubenko LS, Titov YU. Magnetoelectric (Bi, Ln)FeO_3 compounds: crystal growth, structure and properties. *Ferroelectrics* 1994;**162**:11–21.
14. Popov YF, Kadomtseva GP, Vorobev GP, Zvezdin AK. Discovery of the linear magnetoelectric effect in magnetic ferroelectric $BiFeO_3$ in a strong magnetic field. *Ferroelectrics* 1994;**162**:135–40.
15. Chu YH, Martin LW, Holcomb MB, Gajek M, Han SJ, He Q, et al. Electric-field control of local ferromagnetism using a magnetoelectric multiferroic. *Nature Materials* 2008;**7**:478–82.
16. Li J, Wang J, Wuttig M, Ramesh R, Wang N, Ruette B, et al. Dramatically enhanced polarization in (0 0 1), (1 0 1), and (1 1 1) $BiFeO_3$ thin films due to epitaxial-induced transitions. *Applied Physics Letters* 2004;**84**:5261–3.
17. Das RR, Kim DM, Baek SH, Eom CB, Zavaliche F, Yang SY, et al. Synthesis and ferroelectric properties of epitaxial $BiFeO_3$ thin films grown by sputtering. *Applied Physics Letters* 2006;**88**:242904.
18. Ramesh R, Zavaliche F, Chu YH, Martin LW, Yang SY, Cruz MP, et al. Magnetoelectric complex-oxide heterostructures. *Philosophical Magazine Letters* 2007;**87**:155–64.
19. Teague JR, Gerson R, James WJ. Dielectric hysteresis in single crystal $BiFeO_3$. *Solid State Communications* 1970;**8**:1073–4.
20. Park SE, Shrout TR. Ultrahigh strain and piezoelectric behavior in relaxor based ferroelectric single crystals. *Journal of Applied Physics* 1997;**82**:1804–11.
21. Guo R, Cross LE, Park S-E, Noheda B, Cox DE, Shirane G. Origin of the high piezoelectric response in $PbZr_{1-x}Ti_xO_3$. *Physical Review Letters* 2000;**84**:5423–6.
22. Fu H, Cohen RE. Polarization rotation mechanism for ultrahigh electromechanical response in single-crystal piezoelectrics. *Nature* 2000;**403**:281–3.
23. Ahart M, Somayazulu M, Cohen RE, Ganesh P, Dera P, Mao H-K, et al. Origin of morphotropic phase boundaries in ferroelectrics. *Nature* 2008;**451**:545–8.
24. Zeches RJ, Rossell MD, Zhang JX, Hatt AJ, He Q, Yang CH, et al. A strain-driven morphotropic phase boundary in $BiFeO_3$. *Science* 2009;**326**:977–80.
25. Martin LW, Chu YH, Ramesh R. Advances in the growth and characterization of magnetic, ferroelectric, and multiferroic oxide thin films. *Materials Science and Engineering R* 2010;**68**:89–133.
26. Chen Z, You L, Huang C, Qi Y, Wang J, Sritharan T, et al. Nanoscale domains in strained epitaxial $BiFeO_3$ thin films on $LaSrAlO_4$ substrate. *Applied Physics Letters* 2010;**96**:252903.
27. Zhang JX, Xiang B, He Q, Seidel J, Zeches RJ, Yu P, et al. A road to huge strains in lead-free multiferroics through nanoscale phase engineering. *Nature Nanotechnology*; accepted.
28. Ederer C, Spaldin NA. Effect of epitaxial strain on the spontaneous polarization of thin film ferroelectrics. *Physical Review Letters* 2005;**95**:257601.
29. Hoffman MJ, Hammer M, Endriss A, Lupascu DC. Correlation between microstructure, strain behavior, and acoustic emission of soft PZT ceramics. *Acta Materialia* 2001;**49**:1301–10.
30. Ricinschi D, Yun K-Y, Okuyama M. A mechanism for the 150 μCcm^{-2} polarization of $BiFeO_3$ films based on first-principles calculations and new structural data. *Journal of Physics: Condensed Matters* 2006;**18**:L97–105.
31. Infante IC, Lisenkov S, Dupé B, Bibes M, Fusil S, Jacquet E, et al. Bridging multiferroic phase transitions by epitaxial strain in $BiFeO_3$. *Physical Review Letters* 2010;**105**:057601.
32. Hatt AJ, Spaldin NA, Ederer C. Strain-induced isosymmetric phase transition in $BiFeO_3$. *Physical Review B* 2010;**81**:054109.
33. Jiang Q, Qiu JH. The thickness dependence of ferroelectric and magnetic properties in epitaxial $BiFeO_3$ thin films. *Journal of Applied Physics* 2006;**99**:103901.
34. Zhang JX, Li YL, Wang Y, Liu ZK, Chen LQ, Chu YH, et al. Effect of substrate-induced strains on the spontaneous polarization of epitaxial $BiFeO_3$ thin films. *Journal of Applied Physics* 2007;**101**:114105.
35. Ma H, Chen L, Wang J, Ma J, Boey F. Strain effects and thickness dependence of ferroelectric properties in epitaxial $BiFeO_3$ thin films. *Applied Physics Letters* 2008;**92**:182902.
36. Zhang JX, Schlom DG, Chen LQ, Eom CB. Tuning the remanent polarization of epitaxial ferroelectric thin films with strain. *Applied Physics Letters* 2009;**95**:122904.
37. Huang CW, Chu YH, Chen ZH, Wang J, Sritharan T, He Q, et al. Strain-driven phase transitions and associated dielectric/piezoelectric anomalies in $BiFeO_3$ thin films. *Applied Physics Letters* 2010;**97**:152901.
38. Kovachev St, Wesselinowa JM. Influence of substrate effects on the properties of multiferroic thin films. *Journal of Physics: Condensed Matter* 2009;**21**:395901.
39. Li LJ, Li JY, Shu YC, Yen JH. The magnetoelectric domains and cross-field switching in multiferroic $BiFeO_3$. *Applied Physics Letters* 2008;**93**:192506.

40. Li LJ, Yang Y, Shu YC, Li JY. Continuum theory and phase-field simulation of magnetoelectric effects in multiferroic bismuth ferrite. *Journal of the Mechanics and Physics of Solids* 2010;**58**:1613–27.
41. Zhang JX, Li YL, Choudhury S, Chen LQ, Chu YH, Zavaliche F, et al. Computer simulation of ferroelectric domain structures in epitaxial $BiFeO_3$ thin films. *Journal of Applied Physics* 2008;**103**:094111.
42. Shu YC, Yen JH, Shieh J, Yeh JH. Effect of depolarization and coercivity on actuation strains due to domain switching in barium titanate. *Applied Physics Letters* 2007;**90**:172902.
43. Yen JH, Shu YC, Shieh J, Yeh JH. A study of electromechanical switching in ferroelectric single crystals. *Journal of the Mechanics and Physics of Solids* 2008;**56**:2117–35.
44. Shu YC, Yen JH, Chen HZ, Li JY, Li LJ. Constrained modeling of domain patterns in rhombohedral ferroelectrics. *Applied Physics Letters* 2008;**92**:052909.
45. Kuo HY, Shu YC, Chen HZ, Hsueh CJ, Wang CH, Chu YH. Domain pattern and piezoelectric response across polymorphic phase transition in strained bismuth ferrite films. *Applied Physics Letters* 2010;**97**:242906.
46. Shu YC, Bhattacharya K. Domain patterns and macroscopic behavior of ferroelectric materials. *Philosophical Magazine B* 2001;**81**: 2021–54.
47. Chen LQ. Phase-field models for microstructure evolution. *Annual Review of Materials Research* 2002;**32**:113–40.
48. Li YL, Hu SY, Liu ZK, Chen LQ. Effect of substrate constraint on the stability and evolution of ferroelectric domain structures in thin films. *Acta Materilia* 2002;**50**:395–411.
49. James RD. Displacive phase transformations in solids. *Journal of the Mechanics and Physics of Solids* 1986;**34**:359–94.
50. Wang J, Zhang TY. Effect of long-range elastic interactions on the toroidal moment of polarization in a ferroelectric nanoparticle. *Applied Physics Letters* 2006;**88**:182904.
51. Ruszczynski A. *Nonlinear Optimization*. Princeton University Press; 2006.
52. Shu YC, Lin MP, Wu KC. Micromagnetic modeling of magnetostrictive materials under intrinsic stress. *Mechanics of Materials* 2004;**36**: 975–97.